Received: 14 March 2018 | Revised: 5 July 2018 | Accepted: 10 July 2018
DOI: 10.1002/cm.21478

RESEARCH ARTICLE

Strong cytoskeleton activity on millisecond timescales upon particle binding revealed by ROCS microscopy

Felix Jünger[1] | **Alexander Rohrbach**[1,2]

[1]Laboratory for Bio- and Nano-Photonics, Department of Microsystems Engineering, University of Freiburg, Freiburg, Germany

[2]BIOSS Centre for Biological Signalling Studies, Freiburg, Germany

Correspondence
Alexander Rohrbach, Laboratory for Bio- and Nano-Photonics, Department of Microsystems Engineering, University of Freiburg, Freiburg, Germany.
Email: rohrbach@imtek.de

Funding information
University of Freiburg; Deutsche Forschungsgemeinschaft, Grant/Award Number: RO 3615/3

Abstract

Cells change their shape within seconds, cellular protrusions even on subsecond timescales enabling various responses to stimuli of approaching bacteria, viruses or pharmaceutical drugs. Typical response patterns are governed by a complex reorganization of the actin cortex, where single filaments and molecules act on even faster timescales. These dynamics have remained mostly invisible due to a superposition of slow and fast motions, but also due to a lack of adequate imaging technology. Whereas fluorescence techniques require too long integration times, novel coherent techniques such as ROCS microscopy can achieve sufficiently high spatiotemporal resolution. ROCS uses rotating back-scattered laser light from cellular structures and generates a consistently high image contrast at 150 nm resolution and frame rates of 100 Hz—without fluorescence or bleaching. Here, we present an extension of ROCS microscopy that exploits the principles of dynamic light scattering for precise localization, visualization and quantification of the cytoskeleton activity of mouse macrophages. The locally observed structural reorganization processes, encoded by dynamic speckle patterns, occur upon distinct mechanical stimuli, such as soft contacts with optically trapped beads. We find that a substantial amount of the near-membrane cytoskeleton activity takes place on millisecond timescales, which is much faster than reported ever before.

KEYWORDS

actin dynamics, biophysics, coherent imaging, live-cell imaging, superresolution microscopy

1 | INTRODUCTION

The response behavior of living cells upon approaching or contacting particles is a highly complex phenomenon. The interaction between particle and target is a combination of mechanical and biochemical stimuli and responses, which trigger and control each other (Artemenko, Axiotakis Jr., Borleis, Iglesias, & Devreotes, 2016; Orr, Helmke, Blackman, & Schwartz, 2006). Typical response patterns are governed by a complex reorganization of the actin cytoskeleton, which is involved in almost any cellular function including migration, secretion, phagocytosis, cell death (apoptosis) and survival (Papakonstanti & Stournaras, 2008). The actin networks in the cell periphery have been shown to reorganize on subsecond timescales, that is, much faster than the translocation speed of the whole cell (Diez, Gerisch, Anderson, Muller-Taubenberger, & Bretschneider, 2005). The actin reorganization in the cell periphery is coupled to synaptic inputs, that is, the activation of ion channels upon stimulation, and exhibits multiple spatial and temporal patterns (Furuyashiki, Arakawa, Takemoto-Kimura, Bito, & Narumiya, 2002). That means both the stimulus and the response depend strongly on the timescale and length scale of the interaction, or, from a physicist's point of view: the detection bases on a broadband superposition of temporal and spatial frequencies. A diffusing particle is driven by thermal noise and thus offers a broadband spectrum of fluctuations in its position and orientation, which can be measured with three-dimensional high-speed tracking techniques, such as back-focal-plane (BFP) interferometry. The energy transfer of the particle bumping into the cell periphery, which is both dissipative and elastic, can not only vary strongly with the cell type but also with the observed time and length scale (Daddi-Moussa-Ider, Guckenberger, & Gekle, 2016; Jünger et al., 2015). To investigate such broadband interaction, one needs novel imaging methods that are able to resolve small structures (high spatial frequencies) at high frame rates (high temporal frequencies). However, such techniques are more than rare since higher optical resolution requires more photons and more time. In addition, fluorescence bleaching often limits the number of acquired images significantly. Also, when using indirect fluorescent labels such as for example, actin-GFP to visualize actin filaments, its binding rates may become limiting, such that the range of observable velocities is limited and one might therefore underestimate the correct reorganization speeds (Diez et al., 2005).

In a recent paper (Jünger, Olshausen, & Rohrbach, 2016), we reported on a novel high-speed, label-free microscopy method called rotating coherent scattering (ROCS) microscopy, which exploits backscattered rotating laser light to image biological structures. Thousands of acquisitions are recorded with a lossless high image contrast, with a spatial resolution below the diffraction limit and without requiring postprocessing—other than structured illumination microscopy (SIM). We have demonstrated that ROCS microscopy images the cortical cytoskeletal dynamics of living cells with a so far unreached spatiotemporal bandwidth (STBW). For ROCS, this has been of STBW = 63 Hz/(0.15 μm) = 420 Hz/μm over 10,000 frames (Jünger et al., 2016), whereas for a comparable fluorescence-based technique such as SIM one can estimate STBW = 10 Hz/(0.11 μm) ≈ 90 Hz/μm over 100 frames (Allen, Ross, & Davidson, 2014; Kner, Chhun, Griffis, Winoto, & Gustafsson, 2009). Conventional TIR-fluorescence microscopy reaches a STBW = 20 Hz / (0.21 μm) ≈ 95 Hz/μm over 100 frames ((Axelrod, 2001) and references therein) using standard fluorophores such as eGFP and ensuring a low-noise image contrast.

To achieve this performance, ROCS makes use of the principles of coherent imaging. When a biological object is coherently illuminated, the light is scattered at different positions within its dense object structure, such that the scattered partial waves $E_1(t)$, $E_2(t + \tau)$, … have different distances and runtimes τ on their respective way to the camera. Here, the interference of scattered light results in intensity patterns $|E_1 + E_2 + \ldots|^2$ such that either an image of the object is generated if the object structures can be resolved, or the intensity is a nearly random speckle pattern, if the feature sizes are below the resolution limit. This interference pattern is mainly determined by the numerical aperture of the objective lens, the spatial distribution of the scatterers within the sample and the laser wavelength λ. Now, what does the interference pattern help if cellular structures cannot be resolved? As soon as parts of the scattering sample, for example, structures within a biological cell, are moving, additional phase differences within the scattered electromagnetic fields arise, which in consequence result in temporal variations of the speckle patterns. Both the temporal and the spatial statistics of speckle distribution encode information about the dynamics within the sample (Goodman, 1975; Rabal & Braga Jr., 2008).

Although dynamic light scattering (DLS) has been applied in soft matter studies (Hajjarian & Nadkarni, 2012; Meller et al., 1998; Piederrière, Le Meur, Cariou, Abgrall, & Blouch, 2004; Rice et al., 2011) and to investigate biological systems (Briers & Webster, 1996; Hajjarian, Xi, Jaffer, Tearney, & Nadkarni, 2011; Tamaki, Araie, Kawamoto, Eguchi, & Fujii, 1994; Tishler & Carlson, 1987), coherence-based (rather than fluorescence-based) DLS studies of living cells or systems are rare. Our fast and spatially resolved read-out of speckle patterns, however, is a novel and promising method to examine the spatiotemporal evolution of the near-membrane cytoskeleton. The reorganization processes in the cell periphery result mostly from ongoing polymerization and depolymerization of cortical filaments (mainly actin) and changes in their degree of crosslinking. However, these structures are too small to be resolved by conventional light microscopy. Fluorescence-based approaches can image only structures labeled with fluorophores that often hamper the functionality of the protein (e.g., actin-GFP) or reduce the contrast due to unbound fluorophores (Lifeact-GFP) (Belin, Goins, & Mullins, 2014). Fluorescence microscopy techniques are generally relatively slow compared to coherent imaging approaches, although there are established approaches based on fluorescence correlation spectroscopy (Levi, Ruan, Kis-Petikova, & Gratton, 2003) or fluorescence fluctuation analysis (Di Rienzo, 2014) that can probe the diffusion speeds of single specifically labelled molecules in the 3D cellular environment on submillisecond timescales. However, all fluorescence-based techniques involve intrinsic drawbacks such as elaborate fluorophore labeling or transfection, bleaching, phototoxicity and modification of the cell's biochemistry. A review about fluorescent speckle microscopy of cytoskeleton dynamics can be found in (Danuser & Waterman-Storer, 2006). A more recent (also fluorescence-based) study (Meddens & Meddens, 2016) investigates the interplay of cytoskeletal components during podosome organization, but is limited in temporal resolution to acquisition times of $\Delta t \approx 1$–10 s.

In this study, we present a label-free approach offering a high image contrast such that dynamic speckle patterns can be acquired at rates of 63–100 Hz, which is currently limited only by our camera. Herewith, we are able to provide novel insights into the fast dynamics of the actin cytoskeleton in the periphery of J774 macrophages.

Two different ROCS microscope setups were used for this study, where the working principle in combination with optical tweezers is explained in Figure 1 by a sketch and different images from J774 macrophages. ROCS can be used in total internal reflection (TIR) mode or in non-TIR mode (Koch & Rohrbach, 2018), as well as in darkfield (DF) mode or brightfield (BF) mode. Particles (probes) can bind either spontaneously or are moved by optical tweezers in a controlled manner towards the cell periphery. Here, a signal chain is started with a small local stimulus (i.e., a molecular response of the cell's transmembrane receptors), which triggers fast cytoskeleton reorganization needed for the system's response, that is, a reaction of the cell as a whole, such as particle uptake or transport.

The dynamics of cellular structures with varying refractive indices could be well imaged through local constructive and destructive interference intensities on the camera planes of two different ROCS setups. The considerations shown in Figure 1 E explain the quantitative relation between the temporal intensity changes and the spatial dimensions of the observed motion. With the magnification, $M = 63$ of the brightfield ROCS microscope and $M = 100$ of the darkfield TIR-ROCS microscope, respectively, and the physical size of one camera pixel ($\Delta x = \Delta y = \Delta r = 6.45$ μm in both cases), we find $\Delta r' = \Delta r/M = 102$ nm for the brightfield ROCS setup, and $\Delta r' = 64.5$ nm for the darkfield TIR-ROCS microscope. Therefore, a pixel-wise intensity shift $\Delta I(x,y,t)$ can be interpreted as a pixel-wise shift of the structures' positions $\Delta r(x,y,t)$.

The fundamental idea behind our data analysis is to subtract the image (i.e., the two-dimensional intensity distribution $I(x, y, t)$ as measured by the camera) of the scene at a given time t from the image of the same scene at a later time $t + \Delta t$ to see how much the scene has changed within the time interval Δt.

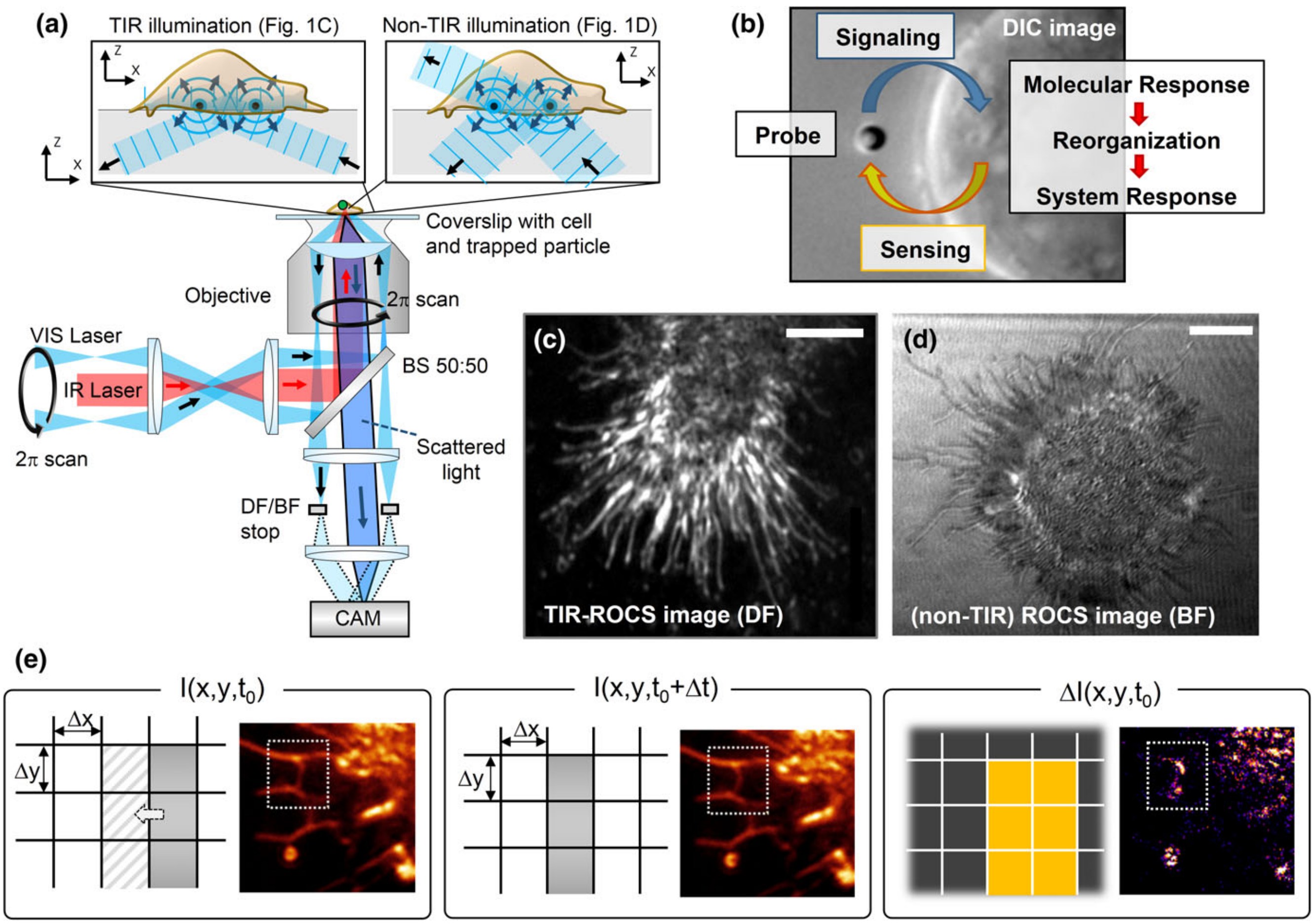

FIGURE 1 (a) Schematic sketch of the experimental setup, both for TIR and non-TIR illumination. A description of the optical components is given in the main text. (b) Conventional brightfield image of a J774 macrophage with a 1 μm polystyrene bead as a probe in the vicinity of the membrane, illustrating the measurement principle, where a bead triggers cytoskeleton reorganization in the cell cortex, resulting in cellular reactions, which are imaged by ROCS. (c) Darkfield (DF) ROCS image of a macrophage (NA = 1,46 objective lens, TIR-ROCS illumination, DF detection, 488 nm laser). (d) Brightfield (BF) ROCS image of a macrophage (NA = 1.2 objective lens, ROCS illumination, without DF aperture in detection beam path, 491 nm laser). Scale bars = 5 μm. (e) Demonstration of the analysis method: The grids represent the pixels on the camera chip with edge lengths Δx and Δy. The measured intensity distribution $I(x,y,t_0)$ results from a lengthy object (green bar) with a refractive index higher than the surrounding and which is displaced by Δx to the left within the time interval Δt. This motion creates an area in the difference image where $\Delta I(x,y,t_0)$ has maximum values (yellow pixels in right frame). In this way, the velocity $v = \Delta x'/\Delta t = \Delta x/M\Delta t$ of the structure can be deduced. The picture insets show a comparable situation in a live cell experiment with a J774 macrophage [Color figure can be viewed at wileyonlinelibrary.com]

The maximum intensity difference ΔI_{max} found in a stack of M images stack is associated with a displacement of $\Delta r' = 64.5$ nm and $\Delta r' = 102$ nm, respectively, and a corresponding velocity $v = \Delta r'/\Delta t$ with units $[v]$ = nm/s. This allows to compute the x-y-position-dependent standard deviation $\sigma_{\Delta I}(x,y,t)$ within a time window of length $m \cdot \Delta t$ at an arbitrary time point t. However, throughout this paper we use the more meaningful velocity standard deviation $\sigma_V(x,y,t)$ expressing the local activity in units nm/s, which is explained in detail in the methods section.

2 | RESULTS

Throughout this study, we used J774 mouse macrophages as an example for cells that exhibit phagocytic activity. Macrophages are components of the mammalian immune system and possess small cell protrusions called filopodia, which for example can act as tentacles to pull bound objects toward the cell to initiate a process called phagocytosis (Kress et al., 2007; Zidovska & Sackmann, 2011). By adding (sub-)μm-sized polystyrene beads to the sample chamber, we induce cellular reactions via signaling processes [mechanical stimulation of the cell's mechanosensitive receptors by the beads (Escude, Rigozzi, & Terentjev, 2014; Jünger et al., 2015; Wang et al., 2005)]. These molecular reactions usually result in a measurable reorganization of the cytoskeleton and lead to the system's response, as depicted in the sketch in Figure 1b.

2.1 | Activity of living and dead cells

Figure 2a,b compares the activity maps of two J774 macrophages calculated by Equation (5) in the Methods section. One of the cells is living and has not received any further treatment, the other one is fixed according to the procedure described in the methods section. The color coding covers the whole range between minimum and maximum activity value as they occur in the whole stack of image differences recorded over 30 s. The activity values occurring at every pixel are given by Equation (5). In addition, the cell activity values are given in relation (in %) to the calculated mean temporal activity of the whole cell.

The living cell (left ROCS image in A and Supporting Information Movie 1) has a temporal resolution defined by the integration time $T_{\text{int}} \approx 20$ ms (see Methods) and exhibits various regions of high activity (Figure 2b left), mostly in the cell cortex, where maximal responsivity of the cell upon stimuli is expected. The highest measured activity is increased by even 171% compared to the mean cellular activity. The measured activity of the fixed cell (right ROCS image in A and Supporting Information Movie 2), however, hardly exhibits any significant differences to the mean value of the whole cell (note the different scaling in Figure 2b). This result is as expected, as no motion neither of the whole cell nor of single cell compartments can occur in fixed cells but demonstrates the applicability of our method. The residual activity of roughly <10% of the mean value is probably due to a drift of the whole sample, remaining thermal motion in the cell and possible instabilities of the illumination laser, which cause apparent (albeit small) speckle dynamics. An additional activity analysis of two living Lifeact-mCherry J774 macrophages, imaged by TIRF microscopy, is presented in the Supporting Information (Supporting Information Figure S1 and Supporting Information Movie 3). The resulting cell activity colocalizes well with the fluorescence signal from filamentous actin and the velocity standard deviations $\sigma_v(x,y,t,f_s)$ show comparable values in the lower frequency range from 0 to 10 Hz to those measured with ROCS. This control experiment is a strong indication that the measured cell activity is indeed a consequence of the rapid reorganization of the actin-rich cytoskeleton.

2.2 | Cell activity on different timescales

Figure 2c shows a single ROCS image with a varying interference intensity, whereas the cell dynamics $\sigma_v(x,y,t,f_s)$ analyzed at an image acquisition rate (sampling rate) of $f_s = 63$ Hz and $\sigma_v(x, y, t, f_s/10)$ at $f_{k\,=\,10}$=6.3 Hz are displayed in Figure 2d (left and middle panel). The latter was obtained by averaging $k = 10$ difference images of the original image stack (see Methods for further details). The time-resolved cell activity is also shown in Supporting Information Movie 4. Combination of both frequency ranges according to Equation (7) yields a meaningful representation of the short-time cell activity between $k_2 = 7$ Hz and $k_1 = 63$ Hz (Figure 2d, right panel). This representation shows that most cellular activity is fast, that is, takes place on short timescales and thus cannot be resolved by slow image acquisition methods.

Fast, non-directional movements would remain hidden at low frame rates $f_s < 7$ Hz due to the long exposure times, which are necessary with most fluorescence techniques to obtain images with a sufficiently low noise level. In other words, these tiny and fast

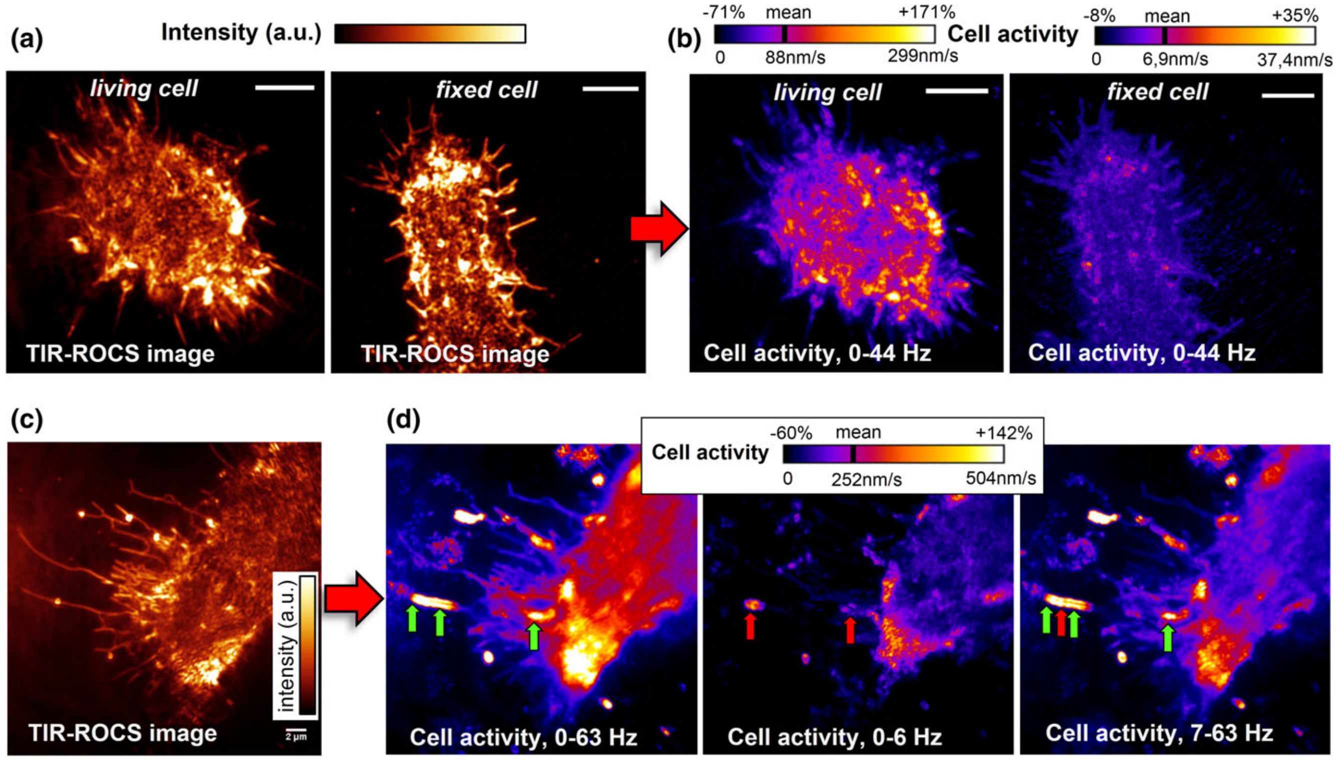

FIGURE 2 (a) Dark field TIR-ROCS images in false color of a living (left) and a fixed (right) J774 macrophage, both acquired at $f_s = 44$ Hz. Color-coded activity maps (b) according to Equation (5) for $m = 60$ subsequent frames (corresponds to 1.36 s). White/yellow areas indicate high cell activity. Scale bars: 5 µm. (c) TIR-ROCS dark field image of a J774 macrophage with a spatial resolution of 150 nm. (d) From left to right: Cell activity $\sigma_v(x,y,t)$ between 0 and 63 Hz, activity map of the same time series downscaled by $k = 10$ to 6.3 Hz, and activity map of the remaining high-frequency part, yielding the cell activity between 7 und 63 Hz. The green arrows point at fast movements that can only be revealed with fast acquisition systems. Red arrows illustrate the information revealed by using slow imaging techniques (<7 Hz) [Color figure can be viewed at wileyonlinelibrary.com]

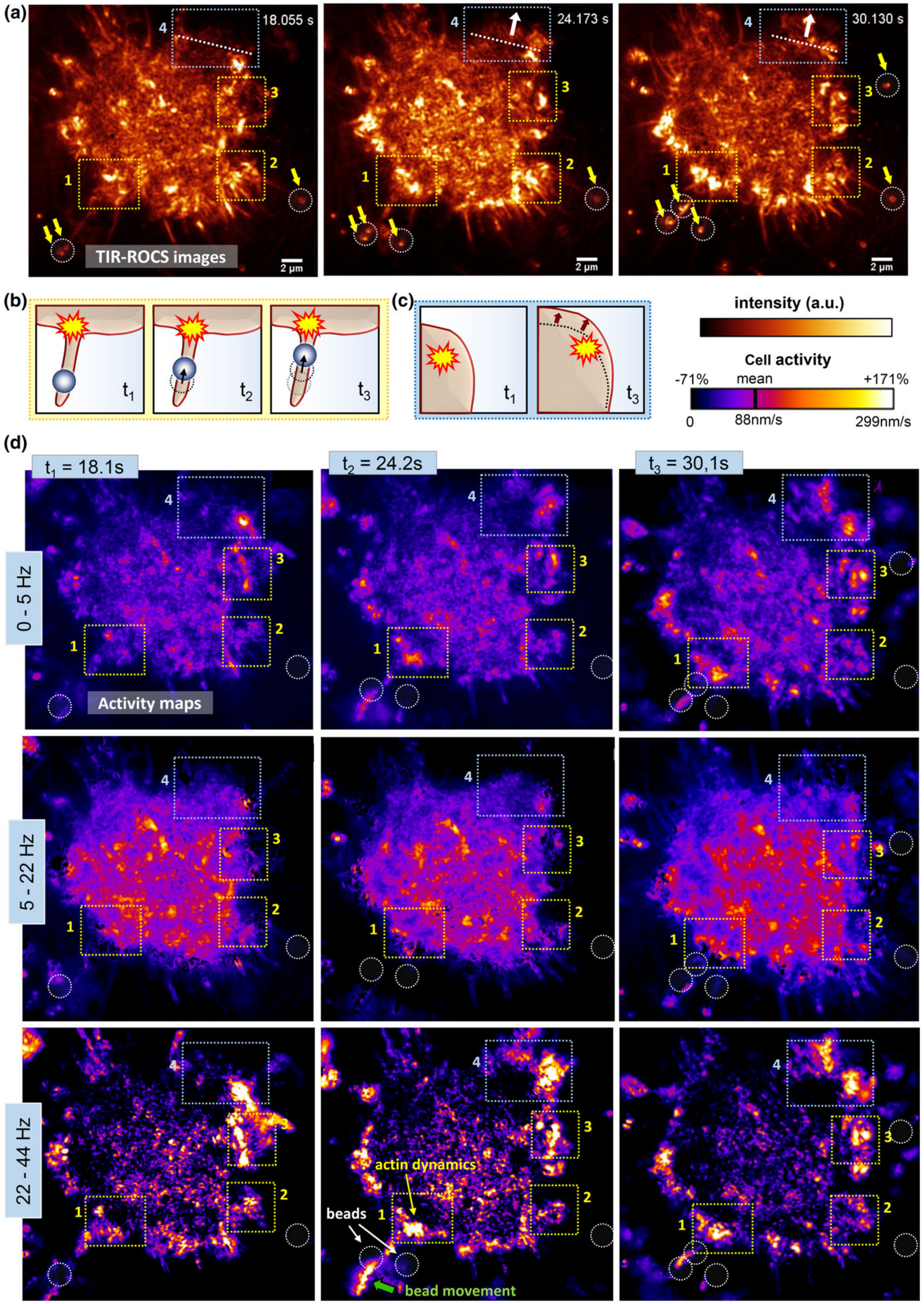
(a)
18.055 s
24.173 s
30.130 s
1
2
3
4
TIR-ROCS images
2 µm
(b)
t1
t2
t3
(c)
t1
t3
intensity (a.u.)
Cell activity
-71%
mean
+171%
0
88nm/s
299nm/s
(d)
t1 = 18.1s
t2 = 24.2s
t3 = 30,1s
0 - 5 Hz
5 - 22 Hz
22 - 44 Hz
Activity maps
actin dynamics
beads
bead movement

FIGURE 3

movements are blurred by motion and their apparent standard deviations appear to be approximately zero, that is, $\sigma_v(x,y,t,6\text{ Hz}) \approx 0$. However, for a sufficiently high sampling frequency f_s, movements in opposite directions can be distinguished and measured as cellular activity on short timescales. This phenomenon is illustrated by the red and green arrows in Figure 2d, which point at a 350 nm-sized glass bead attached to an adherent filopodium. The bead's fast, but non-directional motion ($\sigma_v \approx 0.5$ μm/s) is clearly visible for high frequencies (7–63 Hz, green arrows in D), but remains hidden for <7 Hz (red arrows in middle panel). A similar short-time activity is visible at different positions within the cell cortex.

2.3 | Cell activity during cell motility and during bead transport by adherent filopodia

Macrophages reveal a variety of strategies to take up particles. Besides their engulfment at flat membrane areas or their withdrawal by dorsal filopodia, the roles of adherent filopodia and lamellipodia are especially interesting. Here, beads in contact with the membrane and connected by transmembrane proteins can surf outside the cell towards the cell body, to be taken up a little later (Kohler & Rohrbach, 2015).

Figure 3a shows three snapshots of a darkfield TIR-ROCS time series of a J774 macrophage, recorded at f_s = 44 Hz. Prior to t = 0, which denotes the start of the acquisition, 350 nm small SiO_2 beads have been pipetted into the sample chamber. The beads then settle down to the coverslip due to gravity and by chance interact with the cell's adherent filopodia. Several beads are marked in Figure 3a by yellow arrows and white dotted circles. These beads are then transported in a stop and go manner along the filopodium toward the cell body to initiate particle uptake and phagocytosis (Kohler & Rohrbach, 2015).

From the difference images with $\Delta t = (44\text{ Hz})^{-1}$, the standard deviation of the intensity differences is calculated over m = 60 frames, corresponding to $m \cdot \Delta t$ = 1.36 s. Image sequences were analyzed separately with k = 2 and k = 9 according to Equations (6) and (7), giving rise to three frequency ranges between 0 and 5 Hz ($\leq f_s/9$), between 5 Hz and 22 Hz ($\leq f_s/2$) and between 22 Hz and 44 Hz ($\leq f_s/1$), respectively. The full TIR-ROCS time series together with the time- and frequency-dependent activity maps are also shown in Supporting Information Movie 5. The yellow boxes labelled as '1'–'3' at the periphery of the cell image indicate near-membrane regions at the base of the adherent filopodia, in which strongly increased activities are measured, as can be seen in Figure 3d. This increase corresponds to a threefold increase of σ_v = 88 nm/s to about σ_v = 300 nm/s within a time interval of only 1.36 s. This rise in activity appears most pronounced on the shortest timescales of 45–23 ms (22–44 Hz). In addition, the cell periphery moves north-east, as indicated by the white dotted lines and arrows in Figure 3a. This is probably achieved by actin transport in this direction. The box '4' in Figure 3b exhibits a local, strongly increased activity (up to + 171%) over the course of the whole acquisition series. This increase in cellular activity is broadband, but most pronounced at high frequencies and is probably related to a locally enhanced, fast reorganization of the cytoskeleton.

2.4 | Local cell activity during controlled particle approach

The benefit of a microscope equipped with an optical trap is the possibility to control the approach of particles to living cells. This way, variable cellular reactions are induced, which end up in a measurable reorganization of the near-membrane cytoskeleton, as depicted in Figure 1b. As shown recently (Jünger et al., 2015), we used optical traps with fast interferometric particle tracking to investigate the thermal fluctuations of spherical 1 μm-sized beads in the vicinity of plasma membranes of different living cells. Analysis of the fluctuation data revealed a distance- and direction-dependent viscous drag between membrane and bead surface. The viscous drag or the diffusivity varied strongly, depending on the structures and compositions of the cell interior, the cell coat and the plasma membrane. These variations regulate the physical parameters of the diffusion of an approaching particle, the diffusion times and the stimulation of the cell's mechanosensitive receptors.

Here, we apply the spatially resolved activity analysis (described in the Methods section) as a means to investigate whether the stimulation of macrophages by approaching particles results in a measurable reorganization of the near-membrane cytoskeleton. We approached uncoated 1 μm polystyrene particles, that were optically trapped with a mean lateral fluctuation width of σ = 9 nm (FWHM), in steps of 20 nm. At the end of the approach, the bead was in close contact with the cell membrane.

A typical approach experiment is shown in Figure 4. The bead is approached to a cell with many adherent filopodia along the line marked by the yellow arrow in Figure 4a. Figure 4b displays the cell's activity as calculated with Equation (5) in the whole accessible frequency range between 0 and 100 Hz. The resting filopodia are no longer visible. The first frame at t = 1 s displays the activity at the start of the acquisition, corresponding to 2.0 μm distance between bead surface and cell membrane. In the last frame at t = 31.0 s, the particle approach has ended and bead and cell are in close contact. The white dotted circle surrounding the cell in Figure 4b was used to calculate the mean cellular activity, the smaller dashed white circle beneath the bead contact point represents the ROI, which is tested for increased cell activity in preparation of the particle contact and uptake. In part c

FIGURE 3 Activity analysis of a J774 macrophage handling small glass beads (2R = 350 nm), obtained by an image sequence with f_s = 44 Hz. (a) Darkfield TIR-ROCS images of the cell at three different time points with beads marked by white circles and yellow arrows, revealing two observed processes, which are sketched in (b,c): (b) bead transport along an adherent filopodium and (c) cell cortex movement in north-eastern direction (indicated by white dotted lines and arrows in a). (d) Corresponding frequency-resolved activity maps for three frequency ranges as indicated on the left. The yellow boxes "1"–"3" highlight regions, in which the uptake of several beads via adherent filopodia is initiated (sketch b) and with significantly increased activities on short timescales. The light blue box "4" highlights an area associated with cortex movements, (sketch c) [Color figure can be viewed at wileyonlinelibrary.com]

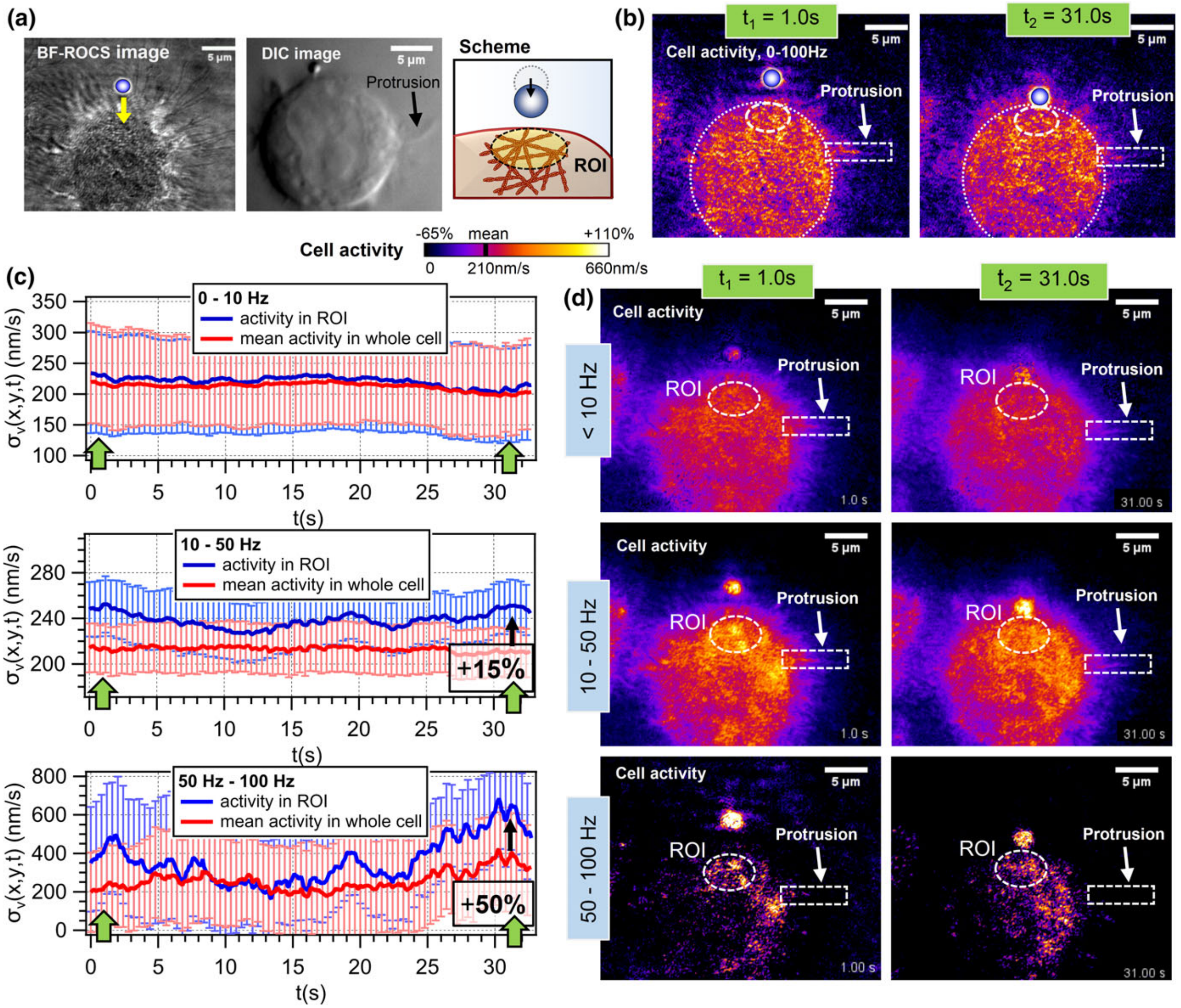

FIGURE 4 Activity analysis of a J774 macrophage during local stimulation. (a) Brightfield ROCS and DIC images of the cell and sketch of the experimental situation. A 1 µm and 50 Hz bead is approached in 20 nm steps toward the cell, coming from the top of the image (yellow arrow in a). The activity of the cytoskeleton is investigated within the whole cell and within a region of interest (ROI) below the membrane. (b) Cell activity in the whole frequency range from 0 to 100 Hz at two different times (beginning [*t* = 1 s] and end [*t* = 31 s] of the particle approach). (c) Time- and frequency-resolved analysis of the cellular activity upon approach of a particle to a J774 cell. From top to bottom: $\sigma_V(x,y,t,f_k)$ calculated in the frequency range from 0 to 10 Hz, 10 to 50 Hz and 50 to 100 Hz, respectively. Red lines denote the average activity in the whole cell, blue curves the activity in the selected ROI. (d) Activity maps for two selected times (beginning and end of the particle approach, see green arrows in c) in three different frequency ranges. The dashed white circle indicates a ROI of increased cytoskeleton activity. Additional arrows and white boxes indicate the location of a moving protrusion, which is causing increased activity in the eastern part of the cell [Color figure can be viewed at wileyonlinelibrary.com]

and d of the figure, a frequency-resolved activity analysis with $k = 2$ and $k = 10$ within time intervals of 1 s is performed, giving access to the frequency ranges 0–10 Hz, 10–50 Hz and 50–100 Hz, respectively. This analysis is also shown in Supporting Information Movie 6.

While the occurring movements and velocities of the cytoskeletal structures appear to be approximately evenly distributed over most parts of the cell in the activity diagrams 0–100 Hz, 0–10 Hz and 10–50 Hz, an increased activity can be identified in the high frequency activity map (>50 Hz). This is most apparent in the upper and right parts underneath the membrane at maximum unidirectional velocities $\sigma_V(x,y,t) = 660$ nm/s (see Figure 4d). A quantitative time-resolved analysis of the activity within the marked ROI and the whole cell average is shown in Figure 4c. For frequencies below 10 Hz, no increase in activity can be measured at any times. On intermediate frequencies between 10 and50 Hz, an increase of the cell activity by 15% is visible. Considering the residual background activity that is measured even for fixed cells due to possible drifts of the experimental setup (see Figure 2), this modest increase is not considered a significant activity rise. However, for frequencies >50 Hz, a significant increase in activity is revealed for times $t > 27$ s, that is, at the final phase of the particle approach shortly before mechanical contact between bead and cell is established. Cytoskeletal movements occurring in this frequency range furthermore exhibit the highest velocities with $\sigma_v \approx 660$ nm/s within 1 s. In addition, an area of increased activity is located on the right side of the cell. Although no approaching particle is visible, we identify a cell protrusion (a dorsal filopodium or a membrane ruffle) on the cell's right (see arrow in the DIC image in [a]), as a probable reason for the high activity in the cortical region, in which the protrusion's actin backbone is embedded.

2.5 | Local cell activity during extracellular bead transport

Figure 5 presents a brightfield ROCS measurement in which a weakly trapped 1 μm polystyrene bead was placed in a distance of now only about 1 μm to the membrane of a J774 macrophage. These kinds of experiments typically result in a binding of the bead to the hardly visible dorsal filopodia of the cell, which then pull the bead toward the cell membrane (see the downward movement of the bead in Figure 5c between 12 s and 20 s). Next, a transport of the bead along the cell membrane can be observed prior to particle internalization. The ROI in Figure 5 depicts the area underneath the cell membrane, which is located in the direction of the bead transport. The cellular activity is analyzed within a time interval of 1 s (corresponding to 100 frames) both for the ROI and the whole cell as a comparison. In the analysis shown in Figure 5d, we omit the low frequency part <10 Hz and focus only on frequencies between 10 Hz and 100 Hz, in which we expect most of the cytoskeleton activity to occur (as shown in Figures 2d and 4).

In the selected ROI, we find an increase in cytoskeleton activity $\sigma_v(x,y,t,f_k)$ for $t \geq 18$ s compared to the average cell activity. This active area is the region towards which the bead is transported. An increase in cytoskeleton activity of up to 44% is observed at $t \geq 27$ s, that is, before the bead is transported to the right. The endpoint of the bead transport along the membrane (at $t = 45$ s) is indicated by

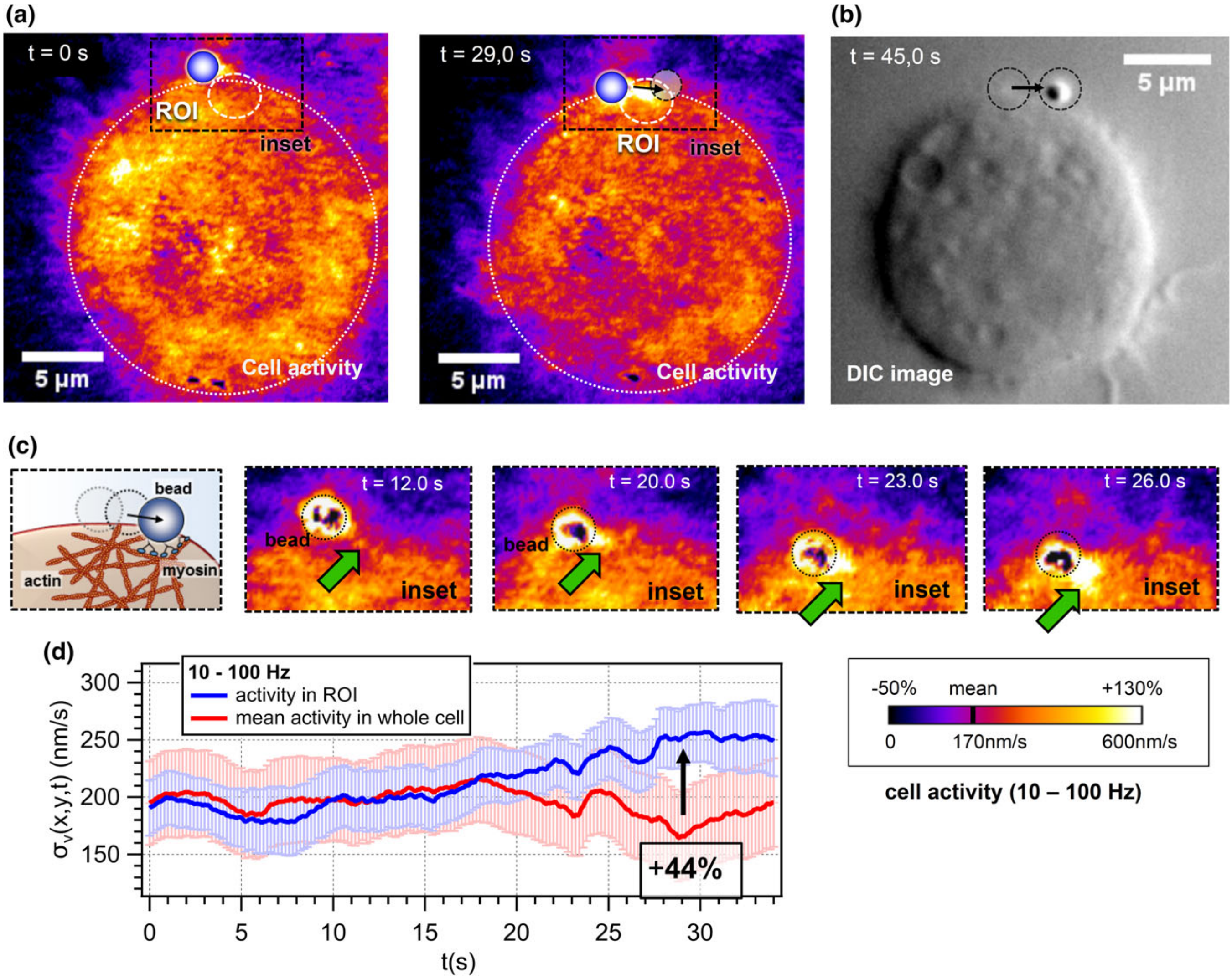

FIGURE 5 Preparation for particle transport. (a) Activity maps on timescales of 10–100 Hz obtained by brightfield ROCS in combination with an optical trap. A bead placed close to the cell membrane, from which the activity is mapped in pseudo colors for different time points (whole cell or inset = black dashed box with bead as a black dotted circle). The grey, semi-transparent bead at $t = 29{,}0$ s denotes the position where the bead is transported to for times $t > 35$ s. (b) DIC image at a later time ($t = 45.0$ s), showing the length of the bead transport. (c) Sketch of the bead transport along the actin-myosin-system underneath the cell membrane. (d) Analysis for cortex motions at 10–100 Hz reveals a change in activity $\sigma_v(x,y,t,f_k)$ in the ROI compared to $\sigma_v(x,y,t,f_k)$ of the whole cell (error bars = standard deviation of the mean) [Color figure can be viewed at wileyonlinelibrary.com]

the gray, semi-transparent bead overlay in Figure 5a and can be clearly identified in the DIC-image (Figure 5b). The experimental observations in connection with Figure 5 indicate that the bead transport along the membrane is achieved by structural reorganizations inside the near-membrane actin-myosin-system. The high activity in front of the bead's trace gives rise to the assumption that the bead is pulled by molecular motors and the cytoskeleton.

2.6 | Fourier-transform based cell activity analysis

Instead of selecting distinct timescales (e.g., >100 ms, 50–20 ms and 20–10 ms in the experiments of Figure 4), it is possible to perform a continuous spectral analysis by a temporal Fourier transform (see Equation (9)). At a central position x_0, we took a vertical line scan (depicted in Figure 6b) from the same experiment as shown in Figure 4 and determined a kymograph $I(y, t)$ and its power spectral density $\mathrm{PSD}(y, f) = |FT[I(y, t)]|^2$, see Equation (9). The kymograph in Figure 6a shows the temporal evaluation of the ROCS image intensity over 20 s, indicating three areas of interest: first, the varying bead position (the brightest trace marked by a white arrow), second, the area ROI1 at the periphery indicating high activity (blue arrow) and third, the area ROI2 as a reference in the central part of the cell (the broad region around the red arrow). In the kymograph and the corresponding inset, the lifetimes τ_{sp} of the speckles can be estimated by the length of a stripe of constant intensity to be in the sub-second range. The $PSD(y, f)$in Figure 6c on the other side shows the temporal frequencies f of the speckles, where a strong decay represents a long lifetime of the speckles and slow dynamics at this point within the cell. Hence, the region indicated by the white arrow shows the broad thermal fluctuation spectrum of the bead, whereas the region of high

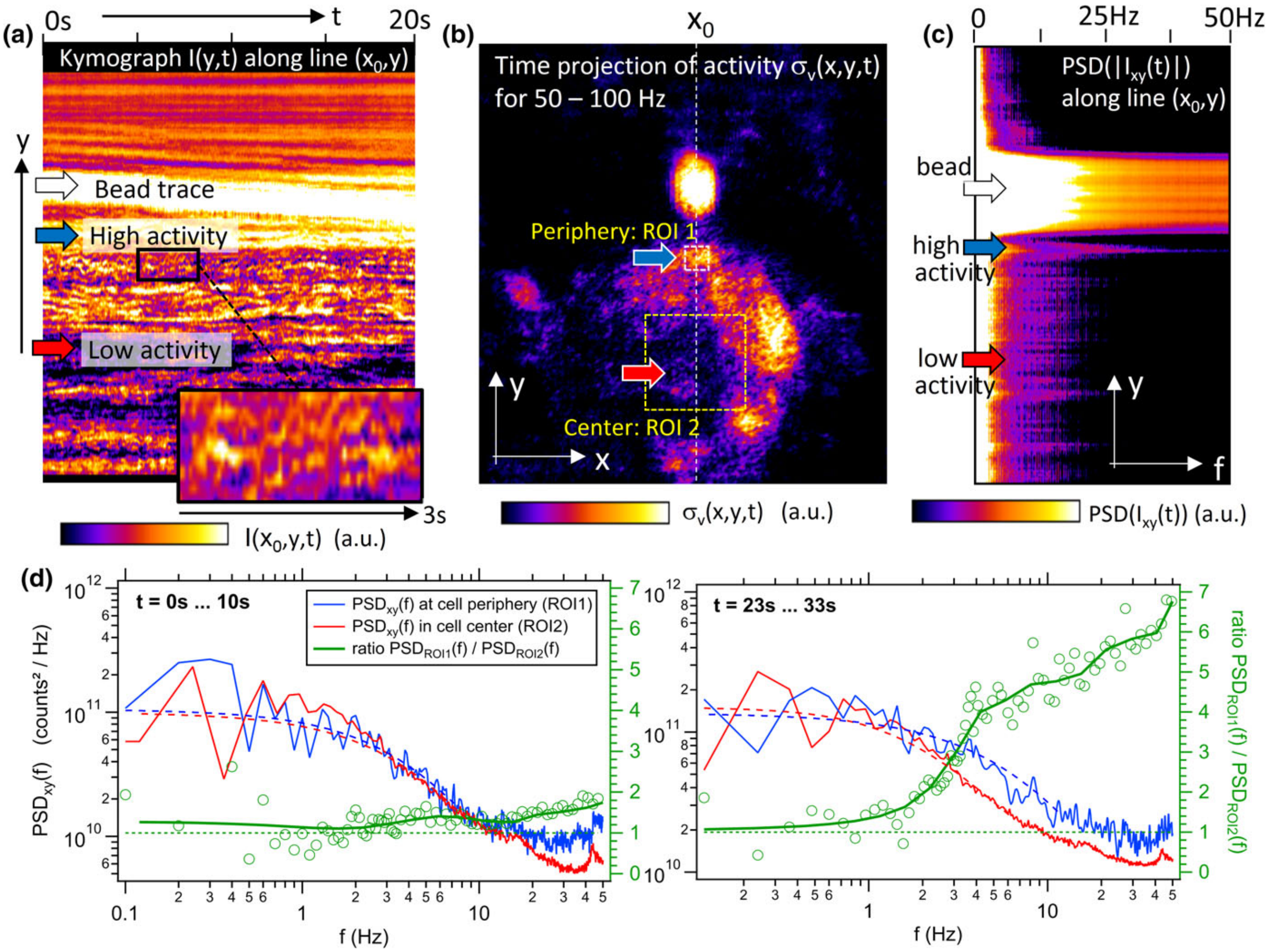

FIGURE 6 Extended frequency-resolved activity analysis of the cell in Figure 4. (a) Kymograph $I(y,t)$ of the bead approach (0–20 s) along the vertical line (x_0,y) in (b). Arrows indicate traces of the strongly scattering bead and of intracellular regions with high and low activity. The black inset illustrates the speckle lifetimes in the sub-second range, deduced from the horizontal extent of the observed spots. (b) Time-projected (0–20s) cellular activity $\sigma_v(x,y,t)$ in the frequency range 50–100 Hz. Two ROIs highlight high activity upon particle approach (ROI 1: Cell periphery) and low activity in the cell center (ROI 2). (c) Logarithmic magnitude of the power spectral density $PSD_{xy}(f) = \mathrm{FT}[|I_{xy}(t)|^2]$ of the kymograph intensity $I(x_0,y,t)$. Arrows indicate dynamics of the bead and within ROIs 1 and 2. (d) $PSD_{xy}(f)$ (left axes) of dynamic processes in the cytoskeleton at the positions of blue and red arrows in (c). Left: Beginning (t = 0 s … 10s), right: End of bead approach (t = 23 s … 33 s). Green markers (right axes) display the ratio of $\mathrm{PSD}_{xy}(f)$ in the cell periphery and $\mathrm{PSD}_{xy}(f)$ in the center. The solid green line represents a cubic spline interpolation of the data points. Red and blue dashed curves are Lorentz fits up to f = 8 Hz, serving as a guide to the eye [Color figure can be viewed at wileyonlinelibrary.com]

activity (blue arrow) close to the approaching bead contains significantly higher frequencies than the reference area within the region ROI2, where temporal changes of the speckles contain only low frequencies. This behavior is further quantified in Figure 6d, where the power spectral densities $PSD(f)$ are plotted for two different positions at the beginning (t = 0 s … 10s) and the end of the bead approach (t = 23 s … 33 s). Here, only the PSDs accounting for local cytoskeletal reorganizations are displayed, while diffusive motion signals have been subtracted. Usually, viscoelastic movements are superimposed by the $1/f^2$ power spectrum of the diffusive, predominantly viscous behavior of the whole cell, thereby obstructing the identification of local processes in the (cumulative) power spectrum. Details of this procedure are discussed in the Supporting Information (see Supporting Information Figures S3, S4 and corresponding text). By plotting the ratio of both corrected PSDs, the relative increase of actin activity close to the bead by a factor of 4 for frequencies around 10 Hz becomes apparent, increasing even to seven-fold at around 50 Hz.

3 | DISCUSSION

3.1 | Necessity of fast image acquisition systems

In this study, we have established a measurement technique based on rotating coherent scattering (ROCS) microscopy, which enables to quantify cellular activity with high spatial resolution (150 nm and 180 nm, for brightfield-ROCS and TIR-darkfield ROCS, respectively). The high frame rate is only limited by the speed of the scan mirror and the camera, allowing up to 100 Hz in this study. We have shown in connection with Figure 2 that the dynamics in the actin-rich cell cortex occurs on all timescales simultaneously but is especially pronounced at high frequencies. In other words, short time differences and thus fast, nondirectional movement cannot be studied with slow imaging techniques, such as for example, epi-fluorescence microscopy, where limited fluorescence emission usually limits the frame rate and the number of acquisitions. (Isambert & Maggs, 1996; Sackmann, 2004) give a course breakdown of the timescales for processes in actin-myosin-networks: The region of slow dynamics (< 1 Hz) covers diffusion and relaxation processes of cell compartments or even whole cells, a region of intermediate dynamics (1–10 Hz) that accounts for deformation of the actin network and a regime of fast dynamics (10–1000 Hz) that includes diffusion and relaxation of single actin filaments and actin monomers. Though this classification may not be transferred that easily to the complex processes occurring in living cells, it still serves as a useful qualitative guidance for the structure dynamics in living cells.

3.2 | Fast cytoskeleton reorganization

The observed dynamics of the speckle fluctuations is determined by the velocities of the scattering structures. Because the highest dynamics is measured in the actin-rich regions of the cell cortex and only the outer cell cortex is accessible with evanescent wave microscopy (to a depth of about 1 μm including scattering), we ascribe the observed high activity mainly to the dynamics of the actin cytoskeleton. The question arises about the sense of the cytoskeletal reorganizations at rates of 100 Hz and faster. Living cells could adapt to the physical laws defining the forces and motion of their cellular components over a period longer than a billion years. What is the advantage of such fast motions, which have not been reported before? This shall be discussed in the following, based on the measured observations.

Actin dynamics becomes visible by the ongoing disassembly or elongation of filaments, which are controlled by formin proteins, by the branching of filaments through Arp2/3 complexes after WASP activation (Bretschneider et al., 2004), and particularly by the connections and disconnections of myosin II protein complexes. Their apparently much faster interplay drives the motion inside the actin cortex, thick membrane ruffles or thin filopodia, lamellipodia and focal adhesions, which play an important role in cell migration. Accumulations of transmembrane proteins physically connect the intracellular cytoskeleton to the cell substrate or extracellular matrix and guide cell propagation, again through highly active polymerization and restructuring or branching of actin filaments. The adhesions themselves constantly undergo structural reorganization due to the activation of mechanosensitive proteins such as Src kinase (Wang et al., 2005). The active regions investigated in Figure 3 (blue box "4") possibly resemble such focal adhesions steering the observed cell propagation in north-eastern direction. Also, the highly dynamic regions observed in Figure 2 can probably be associated with polymerization centers of the actin mesh close to the base layer of the cell, which are particularly "active" on short timescales of $(63\text{ Hz})^{-1}$ (and possibly below). Although single actin monomers are far too small to be resolved by our microscopy approach, their (de-)polymerization at filaments result in changing force patterns and deformations of actin filaments and is therefore related to dynamic structural changes and displacements of the cytoskeleton, which can be monitored indirectly in form of dynamic speckle patterns.

In regions near the membrane that are possibly associated with filopodia that mediate particle uptake, an increase in cytoskeletal activity can be measured. This increase points out ongoing structural reorganization processes that initiate phagocytosis. Figure 4 investigates an example of such a process, which is revealed only by a frequency-resolved activity analysis and is most pronounced on frequencies >50 Hz.

Also, the significantly increased cellular activity occurring together with the bead transport prior to particle uptake (see Figure 5) indicates changes in the cortex structure as a preparation for the myosin-driven bead transport (Otten et al., 2012). The high spatial precision of our method allows to localize the transport dynamics within narrow spatial and temporal limits. This broad, but selective bandwidth allows different interesting observations such that the highest activity occurs in that part of the cytoskeleton that the bead is about to be transported to and—remarkably—prior to transport, which therefore must be based on pulling forces exerted by the surrounding cytoskeleton.

3.3 | Multiple scattering upon deeper penetration depth

When the concentration of scatterers is high and/or the light's penetration depth into the sample is large, many scattering centers are simultaneously illuminated. This leads to multiple scattering of the laser light, which causes many phase and polarization shifts of the scattered light and impedes interpretation and evaluation of the arising speckle patterns (Pine, Weitz, Chaikin, & Herbolzheimer, 1988). While a high concentration of scatterers cannot be circumvented when living cells are investigated, the penetration depth can be tuned by experimental parameters. First, all ROCS measurements are carried out such that the *x*-*y*-plane in focus is as close to the coverslip as possible (thus, the adherent filopodia become visible as in Figure 1c,d). Second, the deflection angle of the scan mirror is chosen as high as possible to achieve a very flat angle of incidence onto the sample, therefore illuminating only a minimal *z* depth of the cell. At the same time, the shallow angle increases the effective NA_{ill} and maximizes the spatial resolution.

The TIR-ROCS activity analyses shown in Figures 2, 4 and 5 exhibit very inhomogeneous distributions of areas with high and low activities, respectively, that can clearly be spatially separated. An arising question is whether multiple scattering occurring with deeper sample illumination might change the activity information, as the accuracy of the quantitative analysis of particle speeds $\sigma_v(x,y,t)$ that was introduced in connection with Figure 1e might depend on the penetration depth of the illumination light. As it relates intensity differences to displacements of cellular structures, it is prone to a systematic underestimation of activity, if the light penetrates deeper into the cell, thus being scattered at multiple cell structures within in the same *x*-*y*-area, which of course do not necessarily move with the same velocities and in the same direction.

In the Supporting Information, we analyzed the decay times of the autocorrelation functions $\mathrm{AC}[I_{xy}(t)]$ according to Equation (10), both for the different illumination schemes (TIR vs. non-TIR) and for the different acquisition frame rates, see Supporting Information Figure S2. We find all autocorrelation times to be of the same order of magnitude, independent of acquisition speed and/or illumination depth. Therefore, we do not consider multiple scattering and the detection of additional shifting structures from deeper layers inside the cell to be detrimental for our analysis.

3.4 | Possible phototoxicity

In our study, a 488 nm laser was used with a beam power of p = 1 mW behind the coverslip. On the level of isolated filaments such as microtubules, no toxic effect was observable after thousands of image acquisitions (Koch & Rohrbach, 2018). On the cellular level, it could be seen in several experiments that the overall activity of the macrophages does not change during illumination [see for example, Figures 4 and 5 and reference (Jünger et al., 2016)].

Illuminating a field of view with a radius of $R \approx 50\ \mu\mathrm{m}$ at p = 1 mW results in an incident intensity of $I = P/(\pi R^2) \approx 12\ \mathrm{mW/cm^2}$. It has been shown (Wagner et al., 2010) that a power density of $100\ \mathrm{mW/\ cm^2}$ at wavelength $\lambda = 511$ nm with constant epi-illumination leads to physiological damage of U373-MG glioblastoma cells only after 1,000 s = 16.7 min. Schneckenburger et al. (Schneckenburger, 2012) report that a critical light dose (where less than 90% of the cells maintain their viability and ability to reproduce themselves) is reached after 100 s of constant epi-illumination at $\lambda = 488$ nm and $I = 100\ \mathrm{mW/\ cm^2}$ for CHO-K1 (Chinese Hamster Ovary) cells. We assume that a similar range of critical light doses is relevant also for the J774 macrophages used in this study. If one considers the much lower illumination intensity in our case together with the fact that the rapid decay of the evanescent field in TIR illumination leads to reduced cell damage (Wagner et al., 2010), we expect that phototoxicity is negligible within our observation times of one to several minutes.

3.5 | Current status and outlook

As discussed in our previous papers, ROCS provides a combination of acquisition speed, image contrast and spatial resolution, which is superior to any other microscopy technique used in live-cell imaging. The temporal evaluation of intensity differences of spatially resolved and non-resolved structures (speckles) allows a quantification of the cytoskeleton activity at each pixel either relative (in %) to the mean activity in the whole cell or in absolute values of the velocity standard deviation $\sigma_v(x,y,t)$ with units nm/s. Furthermore, the technique allows activity analyses for different temporal frequency ranges, albeit within certain limits imposed by the choice of f_s and k (see Equation (6) in the methods section). A substantial amount of cellular activity in the periphery of J774 macrophages takes place on short timescales, that is, high frequencies, and would therefore remain elusive with conventional, usually slower imaging techniques.

As the imaging process is based on scattering at refractive index variations, the technique does not allow to identify certain proteins or structures at the current stage. However, for future modifications of the technique, specific fluorescent labelling of selected structures can be exploited as a complementary method to elucidate the role of specific cellular components in the observed dynamic processes.

By computing temporal autocorrelation functions of the measured intensity $I(x,y,t)$, autocorrelation or relaxation times can be determined to estimate the dynamics of structures based on their local viscous and elastic environment (Aizu & Asakura, 1991; Ruth, 1987). The reliability of those correlation-based methods is often limited by the acquisition speed of the imaging system, making it hardly possible to investigate fast processes that occur on millisecond timescales. For instance, at a given sampling rate $f_s = 1/\Delta t = 100$ Hz, only processes with a speckle correlation time $\tau_0 \geq \tau_{\min} = 2\cdot\Delta t = 20$ ms can be reliably sampled (Nyquist's sampling theorem). Recent studies on laser speckle rheology on weakly absorbing fluids were recorded with a fast sCMOS camera at 945 Hz (Hajjarian & Nadkarni, 2014) or even at 1950 Hz (Nader et al., 2016), but without providing any spatial resolution or imaging. Studies which are comparable to our approach are fluorescence-based with the aforementioned advantages (protein-specific) and drawbacks (slow, subject to bleaching). A recent example is the study of Meddens et al. (Meddens & Meddens, 2016), where spatiotemporal image correlation spectroscopy is used to investigate dynamic spatial patterns and directional movements of cytoskeletal components over the course of 75 min, but only with a very small temporal sampling rate in the range of $\Delta t = 5 - 15$ s.

4 | SUMMARY

In this study, we have presented a novel method to visualize, localize and quantify cytoskeleton activity of living cells on the basis of our recently reported ROCS microscopy method. Label-free imaging with ROCS at spatial resolution of 150/181 nm, depending on the objective's numerical aperture (here NA = 1.46/1.2) and on the used laser wavelength (here 488 nm) allows to investigate the dynamics of differently refracting cellular structures (e.g., cytoskeleton, vesicles, membranes) in the cell periphery over the course of many thousand acquisitions. With its unprecedented spatiotemporal bandwidth, ROCS offers scientists in the field of live cell biology a complementary imaging method applicable to a multitude of model-based microrheological analysis methods, helping to unravel the fast mechanical interplay of cellular components. For selected processes in the periphery of living J774 macrophages, we demonstrated that the temporal evolution of intensity patterns (not necessarily unresolved speckles) encode the dynamics of the actin-rich cytoskeleton. Our results show that a significantly increased cellular activity becomes visible in the periphery of living J774 macrophages upon particle approach, upon bead transport along adherent filopodia, during cell propagation and during bead transport along the membrane prior to uptake. Remarkably, these processes, likely related to ongoing polymerization and reorganization inside the near-membrane actin cytoskeleton, revealed the strongest activity on short timescales, that is, at high frequencies, and would thus remain hidden with conventional low-speed, low-contrast measurement techniques. Using ROCS with shorter laser wavelengths, faster cameras and scan mirrors in combination with specific fluorescence labeling will open an exciting future for various experiments and model-based simulations on the hardly explored small and fast world of living cells.

5 | METHODS

5.1 | Cell preparation

All macrophages were cultured at 37 °C in an atmosphere containing 5% CO_2. During growth and experiments, the cells were suspended in cell medium (Dulbecco's Modified Eagle Medium [DMEM] GlutaMAX, Invitrogen Life Technologies, Carlsbad, CA) with 10% fetal bovine serum added). Prior to each experiment, the cells were detached from the bottom of the cell culture flask and transferred onto a microscope cover glass, which had been sterilized by an autoclave. One benefit of the ROCS technique is that it requires no object staining. None of the cells shown in this study received any additional treatment, except for the fixed cell shown in Figure 2a,b. The fixation procedure includes removal of the cell suspension medium, washing the cells three times in phosphate buffered saline (PBS) without supplements (Biochrom GmbH, Berlin, Germany), incubating the cells for 15 min at T = 37 °C in 2.5 mL 4% paraformaldehyde (PFA) solution, which is then replaced by 2.5 mL PBS at 37 °C right before the experiments.

5.2 | Experimental setup: Experimental setup: Image generation

A fundamental prerequisite for the acquisition of dynamic speckle patterns is the presence of a coherent light source. In the experiments presented in this study, a λ = 488 nm (2214-20SL, JDSU, Milpitas, CA, USA) and a λ = 491 nm (Cobolt Calypso, Cobolt AB, Solna, Sweden) cw laser source with a maximum laser power of p = 5 mW were used. The backscattered light is collected by an sCMOS camera (ORCA-Flash4.0 V2, Hamamatsu, Japan) operating at sampling frame rates f_s = 63–100 Hz. During one image acquisition, the angle of incidence of the laser light is rotated azimuthally by 2π with help of a 2D scan mirror (Newport FSM-200, Newport Spectra-Physics GmbH, Darmstadt, Germany), as described in detail in (Jünger et al., 2016). The total electric emitted by N particles or structures, that is, consisting of N elementary waves with fields E_j, leads to the measured intensity $I(x,y,t) = \int_0^{2\pi} \left| \sum_{n=1}^{N} E_n(x,y,t,\phi) \right| d\phi$. Two different microscope setups were used for this study—one equipped with a NA = 1.46 oil immersion lens (HCX PL Apo, 100×, NA 1.46, oil immersion, Leica Microsystems, Wetzlar, Germany), enabling total internal reflection (TIR)-ROCS illumination with a 1/e penetration depth of about 0.1 μm. Its high NA enables a high spatial resolution $d_{\min}$ below the diffraction limit [$d_{\min}$ = 150 nm at λ = 488 nm, see (Jünger et al., 2016)] if oblique sample illumination at $\beta \approx 70^\circ$ is applied. Furthermore, a dark field diaphragm is placed in the detection beam path, such that only the scattered photons are collected by the camera and image contrast is maximized, but image resolution is decreased by 20%. The second microscope is equipped with a 3D-steerable optical trap, formed by a 2 W Nd:GdVO4 solid-state laser with λ = 1,064 nm (Smart Laser Systems, Berlin, Germany) in combination with a NA = 1.2 water immersion objective (C-Apochromat 63x/1.20 W Corr M27, Carl Zeiss, Jena, Germany), as described in (Jünger et al., 2015). At maximum deflection of the scan mirror, an effective illumination NA_{ill} = 1.1 is achieved. Thus, this microscope setup has no TIR capability and achieves a slightly reduced lateral resolution of $d_{\min}$ = 180 nm using oblique illumination at sinβ = NA_{ill}/1.33 (brightfield ROCS). A simplified sketch of the experimental setups is shown in Figure 1a, illustrating both TIR illumination and epi-illumination without TIR. The resulting differences in the imaging process of both illumination modes are illustrated in Figure 1c,d.

5.3 | Speckle image analysis

The fundamental idea behind our data analysis is to subtract the image (i.e., the two-dimensional intensity distribution $I(x, y, t)$ as measured by the camera) of the scene at a given time t from the image of the same scene at a later time $t + \Delta t$ to see how much the scene has changed within the time interval Δt. As reported in (Chang, Chia, & Yang, 2005; Martí-López, Cabrera, Martínez-Celorio, & González-Peña, 2010), all statistical operations that are used to evaluate speckle patterns are also applicable to their difference images. All image processing is performed with the public domain software ImageJ (Rasband, 1997).

In the following, the total spatio-temporal intensity distribution $I(x,y,t)$ measured by the camera is averaged over the aquisition time Δt and can be described as.

$$I(x,y,t) = \frac{1}{\Delta t} \int_{t-\Delta t}^{t} I'(x,y,t')\, dt' \tag{1}$$

where $I(x, y, t) = I_{act}(x, y, t) + I_{BG}(x, y, t)$ is split up into an active contribution $I_{act}(x,y,t)$, which contains the pure speckle dynamics, and an approximately constant background intensity $I_{BG}(x,y,t)$.

In the case of dark field (DF) detection, $I_{BG}(x,y,t)$ is inherently zero [except for a small contribution of interferences and reflections at the surfaces of the optical elements, which can be removed easily by suitable post-processing, see (Jünger et al., 2016)]. For the brightfield (BF) ROCS measurements with the optical trap, darkfield (DF) detection was not available due to the microscope design. Hence, a non-zero background intensity I_{BG} has to be taken into account, but vanishes for $I_{BG}(x,y,t + \Delta t) \approx I_{BG}(x,y,t)$, when only difference images are considered. The difference intensity of two frames $\Delta I(\mathbf{r}, t + \Delta t) = |I_{act}(\mathbf{r}, t + \Delta t) + I_{BG}(\mathbf{r}, t + \Delta t) - I_{act}(\mathbf{r}, t) - I_{BG}(\mathbf{r}, t)|$ separated by a time difference Δt, therefore reads

$$\Delta I(\mathbf{r},t+\Delta t) \approx |I_{act}(\mathbf{r},t+\Delta t) - I_{act}(\mathbf{r},t)| \tag{2}$$

The acquisition time $\Delta t = T_{int} + T_{read} + T_{ps}$ is the time difference between two image acquisitions and is the sum of the camera integration time T_{int}, the readout time T_{read}, and pausing time T_{ps}. For a modern sCMOS camera in streaming mode, T_{read} and T_{ps} are short, that is, $T_{int} >> T_{read} + T_{ps}$, such that the frame rate $f_s = \frac{1}{\Delta t} \approx T_{int}^{-1}$ determines the temporal resolution $\Delta t = 1/f_s$ of an image sequence. For constant frame rates, $\Delta I(x,y,t)$ is proportional to the difference quotient $\Delta I/\Delta t$, which converges to the temporal derivative $\partial I(x,y,t)/\partial t$ for small time differences $\Delta t \to 0$. Hence, $\Delta I(x,y,t)$ is taken as a measure for the temporal changes of the speckle pattern.

To account for the fact that cellular activity occurs on many different timescales simultaneously, a sequence of difference images $\Delta I(x,y,t)$, containing m frames, is analyzed. Following the ideas of (Boas & Dunn, 2010; Briers & Webster, 1996), we calculate the standard deviation of the intensity differences within these intervals to quantify changes within the temporal window $m \cdot \Delta t$. The time window is then subsequently shifted over the complete stack of N difference images in steps of $\Delta t = 1/f_s$. Thus, a resulting stack ("activity map") of N-m-1 frames with maximum temporal resolution is calculated, each of which displays the standard deviation of the speckle dynamics at a given time t with a high lateral spatial ROCS-resolution of 150 nm (or 180 nm, respectively):

$$\sigma_{\Delta I}(x,y,t) = \sqrt{\frac{1}{m\text{-}1} \cdot \left[\sum_{i=0}^{m\text{-}1} \left(\Delta I(x,y,t+i\Delta t) - \Delta\bar{I}_m(x,y,t+m\Delta t)\right)^2\right]} \tag{3}$$

where the pixel-variant mean value

$$\Delta\bar{I}_m(x,y,t+m\Delta t) = \frac{1}{m}\sum_{j=0}^{m-1} \Delta I(x,y,t+j\Delta t) \tag{4}$$

at time $t+m\Delta t$ corresponds to the average over the last m frames $\Delta I(x,y,t)$. All quantities depend on t, since these operations can be performed at arbitrary times and variable time ranges.

5.4 | Quantification of cellular activity

The underlying principle of ROCS microscopy is the scattering of coherent light at structures with different refractive indices. The observed dynamics in the images is based on rapid movements of these structures. With the magnification $M = 63$ of the brightfield ROCS microscope and $M = 100$ of the darkfield TIR-ROCS microscope, respectively, and the physical size of one camera pixel ($\Delta x = \Delta y = 6.45$ μm in both cases), we can calculate the actual lengths that are imaged onto one pixel. For the brightfield ROCS setup, we find $\Delta x' = \Delta x/M = 102$ nm, and $\Delta x' = 64.5$ nm for the darkfield TIR-ROCS microscope. Therefore, a pixel-wise intensity shift $\Delta I(x,y,t)$ can be interpreted as a pixel-wise shift of the structures' positions $\Delta r(x,y,t)$.

The consideration shown in Figure 1e now yields a quantitative relation between the temporal intensity changes and the spatial dimensions of the observed motion. The maximum intensity difference $\Delta I_{max} = \max(\Delta I[x_0,y_0,t])$ found in the entire stack (for $[x_0,y_0]$ inside the part of the image displaying the cell) is associated with a displacement of $\Delta r' = 64.5$ nm and $\Delta r' = 102$ nm, respectively, and a corresponding velocity $v = \Delta r'/\Delta t$ with units $[v]$ = nm/s.

The maximum intensity difference ΔI_{max} that is used to quantify the displacements has to be determined individually for each recorded stack of difference images. A more meaningful x-y-position-dependent velocity standard deviation expressing the local dynamics in units nm/s is then given by:

$$\sigma_v(x,y,t) = \sigma_{\Delta I}(x,y,t) \cdot \frac{\Delta r'}{\Delta I_{max}} \cdot \frac{1}{\Delta t} = \sigma_{\Delta I}(x,y,t) \cdot \frac{\Delta r'}{\Delta I_{max}} \cdot f_s. \tag{5}$$

5.5 | Cellular dynamics on different frequency ranges

Different frequency ranges can be addressed by reducing the temporal resolution of the imaging system, corresponding to a low-pass filtered measurement. This becomes possible by increasing the camera integration time or by summing up k subsequent images $\int_{t-k\Delta t}^{t} I'(x,y,t')\,dt'$, resulting in the average intensity difference according to Equation (4). Hence, the k times slower image acquisition corresponds to a time resolution $k \cdot \Delta t$ or an acquisition rate $f_k = \frac{1}{k \cdot \Delta t}$. By varying the integer k or the rate f_k, a frequency dependent analysis of the cell's dynamics can be performed. The velocity standard deviation $\sigma_v(x, y, t, f_k)$ (see Equation (5)) of the low-pass filtered intensity time series depends on the adjustable sampling frequency $f_k < f_s$ and is expressed as

$$\sigma_\nu(x,y,t,f_k) = \frac{\Delta r' \cdot f_s}{\Delta I_{max}} \cdot \sqrt{\frac{1}{m/k\text{-}1} \cdot \left[\sum_{i=0}^{m/k\text{-}1} \left(\Delta\bar{I}_i(x,y,t+i\Delta t) - \Delta\bar{I}_m(x,y,t+m\Delta t)\right)^2\right]}. \tag{6}$$

The low-pass filtered, that is, averaged data points $\Delta\bar{I}_i$ are calculated by Equation (4). Furthermore, we exploit the fact that the mean value of $\Delta\bar{I}_i$ within the time $m \cdot \Delta t$ equals $\frac{1}{m/k}\sum_{i=0}^{m/k\text{-}1} \Delta\bar{I}_i(x,y,t+i\Delta t) = \Delta\bar{I}_m(x,y,t+m\Delta t)$. Equation (6) thus corresponds to a cellular activity map with a high spatial resolution and temporal frequencies ranging from 0 to f_s/k.

Any intensity time series $\Delta I(x,y,t)$ recorded with a sampling frequency f_s can be split up into a sum of two parts, one accounting only for low frequencies $f \leq f_k = \frac{1}{k \cdot \Delta t}$ and the one for high frequencies $f > f_k$. We can combine different k-values (with $k \in \mathbb{N}$) and corresponding acquisition times $k_1 \cdot \Delta t$ and $k_2 \cdot \Delta t$, such that $\Delta\bar{I}_{k12}(x,y,t+k_{12}\Delta t) = \Delta\bar{I}_{k1}(x,y,t+k_{12}\Delta t) - \Delta\bar{I}_{k2}(x,y,t+k_{12}\Delta t)$ for $k_1 > k_2$. $\Delta\bar{I}_{ki}$ are again defined by Equation (4) and k_{12} = LCM(k_1,k_2) is the least common multiple of k_1 and k_2.

Now, cellular activity in different frequency ranges $\Delta f_k = f_{k2} - f_{k1}$ can be displayed by downscaling the time series (Equation (4)) and calculating the velocity standard deviation according to

$$\sigma_\nu(x,y,t,f_{k1,}f_{k2}) = \frac{\Delta r' \cdot f_s}{\Delta I_{\max}} \cdot \sqrt{\frac{1}{m/k_{12}\text{-}1} \cdot \left[\sum_{i=0}^{m/k_{12}\text{-}1} \left(\Delta \bar{I}_{k12}(x,y,t+i\Delta t) - \Delta \bar{I}_m(x,y,t+m\Delta t) \right)^2 \right]} \tag{7}$$

Equation (7) now corresponds to a cellular activity map for temporal frequencies ranging from f_s/k_1 to f_s/k_2. Again, we use the equivalence of $\frac{1}{m/k_{12}} \sum_{i=0}^{m/k_{12}\text{-}1} \Delta \bar{I}_{k12}(x,y,t+i\Delta t) = \Delta \bar{I}_m(x,y,t+m\Delta t)$. To illustrate the procedure, we present a simple example with f_s = 100 Hz, k_1 = 10 and k_2 = 4. Now, Equation (5) will calculate the cellular activity map for all frequencies from 0 to 100 Hz, Equation (6) results in activity maps ranging from 0 to 10 Hz (=k_1/f_s) and from 0 to 25 Hz (=k_2/f_s), respectively, while Equation (7) yields the cellular activity between f_1 = 10 Hz and f_2 = 25 Hz.

5.6 | Mean cellular activity

Since the velocity standard deviation varies strongly within a cell, especially at positions nearby external stimuli, we define a mean standard deviation by integrating $\sigma_\nu(x,y,t,f_k)$ over the area of the cell:

$$\sigma_\nu^{mean}(t,f_k) = \frac{1}{A_{\text{cell}}} \iint_{\text{cell}} \sigma_\nu(x,y,t,f_k)\, dxdy \tag{8}$$

This mean activity allows to compare and assess the spatially and temporarily varying activities shown in 'fire' pseudo-colors in the Figures 2–6.

5.7 | Fourier analysis of cellular activity

An alternative and complementary approach to investigate the cellular dynamics on different timescales or frequencies, is to analyze the lifetime of speckles by a temporal Fourier transform. This is possible by cutting a thin slice $\delta(s\text{-}r)$ along a straight line with angle θ, such that a 2D time-dependent intensity kymograph is $I(s, t) = \iint I(x, y, t) \cdot \delta(s - x \cdot \cos\theta - y \cdot \sin\theta) dxdy$. The lifetimes τ_{sp} of the speckles (interference structures) are encoded by the length of the stripes in the kymograph $I(s, t) = c \cdot r(s, t)$ with c being a constant defined by the pixel size and by Δt. The lifetimes can be analyzed either by taking the modulus $\left|I(s,f)\right|$ of the temporal Fourier transform of the kymographs $\tilde{I}(s,f) = \int_{t_0}^{t_n} I(s,t) e^{i2\pi ft} dt$, or by computing a space-resolved power spectrum $PSD(s,f) = \left|\tilde{I}(s,f)\right|^2$, which is obtained by the modulus square

$$PSD(s,f) = a_n \left|\tilde{r}(s,f)\right|^2 = a_n \left| \int_{t_0}^{t_n} r(s,t) e^{i2\pi ft} dt \right|^2, \tag{9}$$

which resembles a Lorentzian $PSD(s,f) \approx a_n \left|\tilde{r}_0(s)\right|^2 \cdot \frac{1}{f^2 - f_c^2(s)}$ with the normalization factor $a_n = \frac{c^2}{t_n - t_0}$. By comparing the decay of $\left|\tilde{I}(s,f)\right|$ or of $PSD(s, f)$ at different positions s within the cell (i.e., within the kymograph), the local cell dynamics can be compared on different frequency ranges. $\tilde{r}_0(s) = \tilde{r}_0(s,0) = \int_{t_0}^{t_n} r(s,t) dt$ corresponds to the mean position signal $I_0(s) = c \cdot \tilde{r}_0(s)$ detected on the camera at position s. According to the Wiener-Khintchine theorem, the inverse Fourier transform of Equation (9) yields the temporal autocorrelation function $AC(I(s,t)) = FT^{-1}\left[\left|\tilde{I}(s,f)\right|^2\right] = g(s,\tau)$ of the speckle intensity distribution.

$$g(s,\tau) = a_n \cdot FT^{-1}\left[\left|\tilde{r}(s,f)\right|^2\right] \approx g_0(s) \cdot \exp(-\tau/\tau_c(s)) \tag{10}$$

In the case of a linear viscoelastic material, the decay of the autocorrelation function is roughly exponential with a space varying relaxation time $\tau_c(s)$, describing the material properties at position s.

ACKNOWLEDGMENTS

The authors gratefully acknowledge helpful comments on the manuscript from Winfried Römer, Birgit Erhard for her assistance with the cell culture and the Deutsche Forschungsgemeinschaft (DFG) for financial funding, grant RO 3615/3. This study was supported by the BIOSS Centre for Biological Signalling Studies, University of Freiburg.

AUTHOR CONTRIBUTIONS

F.J. performed the experiments, acquired and analyzed the data. A.R. initiated and supervised the project and designed the experimental setups. F.J. and A.R. interpreted the data, prepared the figures and wrote the manuscript.

REFERENCES

Aizu, Y. A., & Asakura, T. (1991). Bio-speckle phenomena and their application to the evaluation of blood flow. *Optics & Laser Technology*, *23*(4), 205–219.

Allen, J. R., Ross, S. T., & Davidson, M. W. (2014). Structured illumination microscopy for superresolution. *Chemphyschem*, *15*(4), 566–576.

Artemenko, Y., Axiotakis, L., Jr., Borleis, J., Iglesias, P. A., & Devreotes, P. N. (2016). Chemical and mechanical stimuli act on common signal transduction and cytoskeletal networks. *Proceedings of the National Academy of Sciences*, *113*(47), E7500–E7509.

Axelrod, D. (2001). Total internal reflection fluorescence microscopy in cell biology. *Traffic*, *2*(11), 764–774.

Belin, B. J., Goins, L. M., & Mullins, R. D. (2014). Comparative analysis of tools for live cell imaging of actin network architecture. *BioArchitecture*, *4*(6), 189–202.

Boas, D. A., & Dunn, A. K. (2010). Laser speckle contrast imaging in biomedical optics. *Journal of Biomedical Optics*, *15*(1), 011109.

Bretschneider, T., Diez, S., Anderson, K., Heuser, J., Clarke, M., Müller-Taubenberger, A., … Gerisch, G. (2004). Dynamic actin patterns and Arp2/3 assembly at the substrate-attached surface of motile cells. *Current Biology*, *14*(1), 1–10.

Briers, J. D., & Webster, S. (1996). Laser speckle contrast analysis (LASCA): A nonscanning, full-field technique for monitoring capillary blood flow. *Journal of Biomedical Optics*, *1*(2), 174–179.

Chang, C.-C., Chia, T.-L., & Yang, C.-K. (2005). Modified temporal difference method for change detection. *Optical Engineering*, *44*(2), 027001–027001-10.

Daddi-Moussa-Ider, A., Guckenberger, A., & Gekle, S. (2016). Long-lived anomalous thermal diffusion induced by elastic cell membranes on nearby particles. *Physical Review E*, *93*(1), 012612.

Danuser, G., & Waterman-Storer, C. M. (2006). Quantitative fluorescent speckle microscopy of cytoskeleton dynamics. *Annual Review of Biophysics and Biomolecular Structure*, *35*, 361–387.

Di Rienzo, C., Gratton , E., Beltram , F., & Cardarelli , F. (2014). Probing short-range protein Brownian motion in the cytoplasm of living cells. *Nature Communications*, *5*, 5891.

Diez, S., Gerisch, G., Anderson, K., Muller-Taubenberger, A., & Bretschneider, T. (2005). Subsecond reorganization of the actin network in cell motility and chemotaxis. *Proceedings of the National Academy of Sciences of the United States of America*, *102*(21), 7601–7606.

Escude, M., Rigozzi, M. K., & Terentjev, E. M. (2014). How cells feel: Stochastic model for a molecular Mechanosensor. *Biophysical Journal*, *106*(1), 124–133.

Furuyashiki, T., Arakawa, Y., Takemoto-Kimura, S., Bito, H., & Narumiya, S. (2002). Multiple spatiotemporal modes of actin reorganization by NMDA receptors and voltage-gated Ca2+ channels. *Proceedings of the National Academy of Sciences*, *99*(22), 14458–14463.

Goodman, J. W. (1975). *Statistical properties of laser speckle patterns. In Laser speckle and related phenomena* (pp. 9–75). New York, NY: Springer.

Hajjarian, Z., & Nadkarni, S. K. (2012). Evaluating the viscoelastic properties of tissue from laser speckle fluctuations. *Scientific Reports*, *2*, 316.

Hajjarian, Z., & Nadkarni, S. K. (2014). Correction of optical absorption and scattering variations in laser speckle rheology measurements. *Optics Express*, *22*(6), 6349–6361.

Hajjarian, Z., Xi, J., Jaffer, F. A., Tearney, G. J., & Nadkarni, S. K. (2011). Intravascular laser speckle imaging catheter for the mechanical evaluation of the arterial wall. *Journal of Biomedical Optics*, *16*(2), 026005–026005-7.

Isambert, H., & Maggs, A. (1996). Dynamics and rheology of actin solutions. *Macromolecules*, *29*(3), 1036–1040.

Jünger, F., Kohler, F., Meinel, A., Meyer, T., Nitschke, R., Erhard, B., & Rohrbach, A. (2015). Measuring local viscosities near plasma membranes of living cells with photonic force microscopy. *Biophysical Journal*, *109*(5), 869–882.

Jünger, F., Olshausen, P. V., & Rohrbach, A. 2016. Fast, label-free super-resolution live-cell imaging using rotating coherent scattering (ROCS) microscopy. *Scientific Reports*, *6*.

Kner, P., Chhun, B. B., Griffis, E. R., Winoto, L., & Gustafsson, M. G. L. (2009). Super-resolution video microscopy of live cells by structured illumination. *Nature Methods*, *6*(5), 339–342.

Koch, M., & Rohrbach, A. (2018). Label-free imaging and bending analysis of microtubules by ROCS microscopy and optical trapping. *Biophysical Journal*, *114*(1), 168–177.

Kohler, F., & Rohrbach, A. (2015). Surfing along Filopodia: A particle transport revealed by molecular-scale fluctuation analyses. *Biophysical Journal*, *108*(9), 2114–2125.

Kress, H., Stelzer, E. H. K., Holzer, D., Buss, F., Griffiths, G., & Rohrbach, A. (2007). Filopodia act as phagocytic tentacles and pull with discrete steps and a load-dependent velocity. *Proceedings of the National Academy of Sciences*, *104*, 11633–11638.

Levi, V., Ruan, Q., Kis-Petikova, K., Gratton, E. (2003). Scanning FCS, a novel method for three-dimensional particle tracking. *Biochem Soc Trans*, (Pt 5), 997–1000.

Martí-López, L., Cabrera, H., Martínez-Celorio, R. A., & González-Peña, R. (2010). Temporal difference method for processing dynamic speckle patterns. *Optics Communications*, *283*(24), 4972–4977.

Meddens, M. B., Pandzic, E., Slotman, J. A., Guillet, D., Joosten, B., Meddens, M. B., … Cambi, A. 2016. Actomyosin-dependent dynamic spatial patterns of cytoskeletal components drive mesoscale podosome organization. *Nature Communications*, *7*, 13127.

Meller, A., Bar-Ziv, R., Tlusty, T., Moses, E., Stavans, J., & Safran, S. A. (1998). Localized dynamic light scattering: A new approach to dynamic measurements in optical microscopy. *Biophysical Journal*, *74*(3), 1541–1548.

Nader, C. A., Pellen, F., Roquefort, P., Aubry, T., le Jeune, B., le Brun, G., & Abboud, M. (2016). Evaluation of low viscosity variations in fluids using temporal and spatial analysis of the speckle pattern. *Optics Letters*, *41*(11), 2521–2524.

Orr, A. W., Helmke, B. P., Blackman, B. R., & Schwartz, M. A. (2006). Mechanisms of mechanotransduction. *Developmental Cell*, *10*(1), 11–20.

Otten, M., Nandi, A., Arcizet, D., Gorelashvili, M., Lindner, B., & Heinrich, D. (2012). Local motion analysis reveals impact of the dynamic cytoskeleton on intracellular subdiffusion. *Biophysical Journal*, *102*(4), 758–767.

Papakonstanti, E., & Stournaras, C. (2008). Cell responses regulated by early reorganization of actin cytoskeleton. *FEBS Letters*, *582*(14), 2120–2127.

Piederrière, Y., Le Meur, J., Cariou, J., Abgrall, J. F., & Blouch, M. T. (2004). Particle aggregation monitoring by speckle size measurement; application to blood platelets aggregation. *Optics Express*, *12*(19), 4596–4601.

Pine, D., Weitz, D. A., Chaikin, P. M., & Herbolzheimer, E. (1988). Diffusing wave spectroscopy. *Physical Review Letters*, *60*(12), 1134–1137.

Rabal, H. J., & Braga, R. A., Jr. (2008). *Dynamic laser speckle and applications*. Boca Raton, FL: CRC Press.

Rasband, W. (1997). *ImageJ software* (Vol. 2012). Bethesda, MD: National Institutes of Health.

Rice, T. B., Konecky, S. D., Mazhar, A., Cuccia, D. J., Durkin, A. J., Choi, B., & Tromberg, B. J. (2011). Quantitative determination of dynamical properties using coherent spatial frequency domain imaging. *JOSA A*, *28*(10), 2108–2114.

Ruth, B. (1987). Superposition of two dynamic sipeckle patterns: An application to non-contact blood flow measurements. *Journal of Modern Optics*, *34*(2), 257–273.

Sackmann, E. (2004). Mikromechanik der Zelle. *Physik Journal*, *3*(2), 35–42.

Schneckenburger, H., Weber, P., Wagner, M., Schickinger, S., Richter, V., Bruns, T., … Wittig, R.. 2012. Light exposure and cell viability in fluorescence microscopy. *Journal of Microscopy*, *245*(3), 311–318.

Tamaki, Y., Araie, M., Kawamoto, E., Eguchi, S., & Fujii, H. (1994). Noncontact, two-dimensional measurement of retinal microcirculation using laser speckle phenomenon. *Investigative Ophthalmology & Visual Science*, *35*(11), 3825–3834.

Tishler, R. B., & Carlson, F. D. (1987). Quasi-elastic light scattering studies of membrane motion in single red blood cells. *Biophysical Journal*, *51*(6), 993–997.

Wagner, M., Weber, P., Bruns, T., Strauss, W. S. L., Wittig, R., & Schneckenburger, H. (2010). Light dose is a limiting factor to maintain cell viability in fluorescence microscopy and single molecule detection. *International Journal of Molecular Sciences*, *11*(3), 956–966.

Wang, Y., Botvinick, E. L., Zhao, Y., Berns, M. W., Usami, S., Tsien, R. Y., & Chien, S. (2005). Visualizing the mechanical activation of Src. *Nature*, *434*(7036), 1040–1045.

Zidovska, A., & Sackmann, E. (2011). On the mechanical stabilization of Filopodia. *Biophysical Journal*, *100*(6), 1428–1437.

SUPPORTING INFORMATION

Additional supporting information may be found online in the Supporting Information section at the end of the article.

How to cite this article: Jünger F, Rohrbach A. Strong cytoskeleton activity on millisecond timescales upon particle binding revealed by ROCS microscopy. *Cytoskeleton*. 2018;1–15. https://doi.org/10.1002/cm.21478